

## Article

# Distinguishing Saharan Dust Plume Sources in the Tropical Atlantic Using Elemental Indicators

Daniel E. Yeager<sup>1,2,\*</sup> and Vernon R. Morris<sup>1,3,\*</sup><sup>1</sup> NOAA Center for Atmospheric Sciences, Howard University, Washington, DC 20009, USA<sup>2</sup> The Aerospace Corporation, Chantilly, VA 20151, USA<sup>3</sup> School of Mathematical and Natural Sciences, Arizona State University, Phoenix, AZ 85069, USA

\* Correspondence: daniel.e.yeager@aero.org (D.E.Y.); vernon.morris@asu.edu (V.R.M.)

**Abstract:** The Sahara Desert is the largest contributor of global atmospheric dust aerosols impacting regional climate, health, and ecosystems. The climate effects of these dust aerosols remain uncertain due, in part, to climate model uncertainty of Saharan source region contributions and aerosol microphysical properties. This study distinguishes source region elemental signatures of Saharan dust aerosols sampled during the 2015 Aerosols Ocean Sciences Expedition (AEROSE) in the tropical Atlantic. During the 4-week campaign, cascade impactors size-dependently collected airborne Saharan dust particulate upon glass microfiber filters. Inductively Coupled Plasma Mass Spectrometry (ICP-MS) analysis differentiated metal isotope concentrations within filter samples from various AEROSE dust sampling periods. Back-trajectory analysis and NOAA satellite aerosol optical depth retrievals confirmed source regions of AEROSE '15 dust samples. Pearson correlational statistics of source region activity and dust isotope concentrations distinguished the elemental signatures of North African potential source areas (PSAs). This study confirmed that elemental indicators of these PSAs remain detectable within dust samples collected far into the marine boundary layer of the tropical Atlantic. Changes detected in dust elemental indicators occurred on sub-weekly timescales across relatively small sampling distances along the 23W parallel of the tropical Atlantic. PSA-2 emissions, covering the western coast of the Sahara, were very strongly correlated ( $R^2 > 0.79$ ) with Ca-44 isotope ratios in AEROSE dust samples; PSA-2.5 emissions, covering eastern Mauritania and western Mali, were very strongly correlated with K-39 ratios; PSA-3 emissions, spanning southwestern Algeria and eastern Mali, were very strongly correlated with Fe-57 and Ti-48 ratios. The abundance of Ca isotopes from PSA-2 was attributed to calcite minerals from dry lakebeds and phosphorous mining activities in Western Sahara, based on source region analysis. The correlation between K isotope ratios and PSA-2.5 was a likely indicator of illite minerals near the El Djouf Desert region, according to corroboration with mineral mapping studies. Fe and Ti ratio correlations with PSA-3 observed in this study were likely indicators of iron and titanium oxides from Sahelian sources still detectable in Atlantic Ocean observations. The rapid changes in isotope chemistry found in AEROSE dust samples provide a unique marker of Saharan source regions and their relative contributions to desert outflows in the Atlantic. These elemental indicators provide source region apportionments of Sahara Desert aerosol flux and deposition into the Atlantic Ocean, as well as a basis for model and satellite validation of Saharan dust emissions for regional climate assessments.

**Keywords:** mineral dust aerosols; Saharan dust; air quality; ICP-MS; HYSPLIT; AEROSE

**Citation:** Yeager, D.E.; Morris, V.R. Distinguishing Saharan Dust Plume Sources in the Tropical Atlantic Using Elemental Indicators. *Atmosphere* **2024**, *15*, 554. <https://doi.org/10.3390/atmos15050554>

Academic Editor: Chang H. Jung

Received: 27 February 2024

Revised: 19 April 2024

Accepted: 23 April 2024

Published: 30 April 2024



**Copyright:** © 2024 by the authors. Licensee MDPI, Basel, Switzerland. This article is an open access article distributed under the terms and conditions of the Creative Commons Attribution (CC BY) license (<https://creativecommons.org/licenses/by/4.0/>).

## 1. Introduction

The Sahara Desert is the largest single-emitter of dust aerosols, globally, with atmospheric emissions in the range of 600–1000 Tg/yr [1–3]. Topographic lows containing fluvial sediments from extinct waterways and basins create natural sources for desert aerosol emissions across the nine million km<sup>2</sup> desert [4]. These aerosols, suspended by trade winds and dry convection in the Sahara, travel thousands of kilometers from their source within

the hot and dry Saharan Air Layer (SAL), residing at roughly 1–5 km in altitude [5,6]. Many of these dust aerosols enter the Atlantic Ocean and surrounding regions as the SAL overrides the cooler Atlantic marine boundary layer [7].

There are numerous climate and health implications associated with these dust emissions, driving the need for in situ and remote observations. Saharan dust aerosols directly affect climate through scattering and absorption of solar and terrestrial radiation [8]. Semi-direct and indirect climate effects can occur as dust particles alter cloud formation through temperature changes caused by absorption of solar radiation and cloud ice nucleation, respectively [9,10]. Additionally, the bioavailable nutrients from settling dust aerosols can impact oceanic carbon cycling [11]. Numerous studies have also linked prolonged exposure to Saharan dust emissions with upper respiratory and cardiovascular illnesses [12,13].

Accurate estimates of the changes in composition and size of these dust aerosols improve the prediction of their environmental effects. These silicate-based aerosols contain various amounts of clay minerals, carbonates, iron oxides, titanium oxides, feldspars, and trace metals that largely depend upon the Saharan source region [14,15]. Dust aerosol mineralogy and size determine its optical characteristics, such as refractive index and extinction coefficient, that define its global radiative forcing effects [16–18]. Notably, dust refractive indexes can vary by an order of magnitude in global models due to unresolved heterogeneity in dust aerosol size and composition [19]. During its deposition into the Atlantic Ocean, the iron and phosphorous content within mineral dust can serve as limiting nutrients for microalgae *Sargassum* and phytoplankton growth, impacting oceanic productivity and carbon cycling [20–22]. The composition of mineral dust is also of health and environmental consequence due to its potential toxicity and bioaccumulation in downwind receptor sites [12,13,23]. These implications underscore the importance of in situ measurements in the tropical Atlantic that uniquely characterize the chemical and microphysical evolution of Saharan dust aerosols with minimal contributions from downwind surface emissions.

This investigation addresses two key research questions: (I) How do Saharan dust aerosols evolve (age) with respect to particle microphysics and elemental characteristics during atmospheric transport across the Atlantic? (II) What source-specific elemental markers remain detectable in Saharan dust plumes crossing the Atlantic? To address these questions, this study distinguishes source region elemental signatures of Saharan dust aerosols sampled in the tropical Atlantic during the 2015 Aerosol Ocean Sciences Expedition (AEROSE).

By identifying source-specific elemental markers in desert outflows, a basis for model and satellite validation of regional desert aerosol flux and its Atlantic Ocean deposition can be achieved. Elemental isotope markers in downwind dust aerosol samples can characterize regional precursors of Saharan dust emission activity, advancing the prediction of dust-climate feedback effects [24,25]. This technique can also distinguish anthropogenic sources of dust emissions related to mining, industrial, agricultural, and other land-usage practices, shown to be chemically detectable at SAL receptor sites [26,27]. Previous studies have established broad potential source areas (PSAs) for annual Saharan dust emission [28,29], but refinement and geochemical fingerprinting of these PSAs are necessary to distinguish their downwind contributions and environmental implications.

In the following sections, we discuss the AEROSE campaign and methodologies for elemental differentiation of Saharan dust sources encountered during the campaign; this includes dust aerosol sampling and elemental isotope analysis of sampled particulate matter (PM). We also discuss techniques for the detection of dust intrusions encountered during the campaign and the quantification of their source region contributions. Lastly, we evaluate the relationships between source region contributions and elemental characteristics of AEROSE '15 dust samples.

## 2. Materials and Methods

### 2.1. AEROSE Campaign Overview

AEROSE is a series of ship campaigns designed to characterize African aerosol evolution, understand the Atlantic climate effects of African aerosol intrusions, and improve regional satellite observations and climate models [30,31]. The AEROSE campaign is one of few ocean-based research campaigns with a full suite of in situ, vertical profiling, and radiometric aerosol measurement capabilities. AEROSE collaborates with the Pilot Research Moored Array in the Tropical Atlantic-Northeast Extension (PNE) project. PNE is a joint effort between the United States, France, and Brazil to maintain and expand moored buoys that retrieve critical measurements of oceanic and maritime meteorological conditions [32].

The 2015 AEROSE/PNE campaign began aboard the NATO *Alliance* research vessel in the Canary Islands on 15 November, with an initial southwestward path towards the first mooring located at approximately 20° N, 38° W, that was reached on 20 November, as shown in Figure 1.

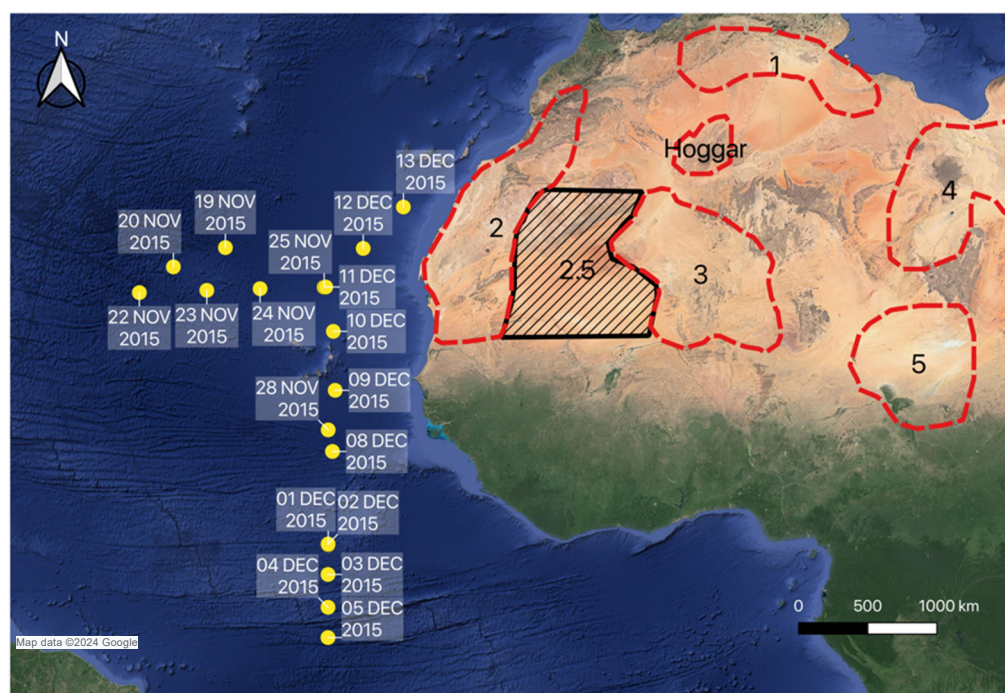


**Figure 1.** AEROSE '15 sampling locations by date, shown in yellow dots with captions. Sahara Desert Potential Source Areas (PSAs) 1–5, PSA-Hoggar, and the added PSA-2.5 are also shown in red and black borders across north Africa. The PSAs cover the following domains: PSA-1: northeastern Algeria and Tunisia, PSA-2: Western Sahara and southern Morocco, PSA-2.5: El Djouf Desert, PSA-3: eastern Mali, southern Algeria, and western Niger, PSA-4: Tibesti Massif, PSA-5: Bodélé Depression and Chad Basin, and PSA-Hoggar: Hoggar Mountains. Map data were provided by ©2024 Google.

After reaching the first mooring site on November 20th, the NATO *Alliance* headed eastward to the second mooring site at approximately 20° N, 23° W, which was reached on November 25th. The RV then headed southward along the 23° W parallel from 25 November to 6 December, where the *Alliance* reached its southernmost point of the cruise at approximately 2S. Three more moorings, two US and one French, were transected along this southern leg of the cruise. The *Alliance* made its northward return to port, mostly along the 23° W parallel, from 6 December to 13 December.

## 2.2. Aerosol Sampling and Elemental Analysis

### 2.2.1. Cascade Impactor

One-stage and Six-stage Staplex cascade impactor air samplers were deployed throughout the AEROSE '15 campaign for size-dependent collection of aerosol particulate matter upon glass microfiber filters (Staplex filter model TFAGF247). This sampling method mainly captured clay fraction mineral dust less than 2  $\mu\text{m}$  in diameter (D). Due to its long atmospheric lifetime, clay fraction mineral dust may account for nearly half of the dust aerosol optical depth and 15% of the atmospheric dust load [17]. The PM-2.5 dust aerosols are also of significant importance and uncertainty from a human health perspective [12], justifying campaign investigations of its microphysical characteristics in long-range transport.

The cascade impactor, shown in Figure 2, uses a vacuum pump to draw in air flow through a series of stages that gradually decrease in nozzle diameter. Due to inertial flow, larger particles are incrementally inhibited from passing to lower stages. In total, 10  $\mu\text{m}$  and 2.5  $\mu\text{m}$  pre-impactors were utilized throughout air sampling to discriminate against larger non-dust aerosols. The two-stage air sampler allowed for size-dependent cutoffs in aerosol collection at 0.8  $\mu\text{m}$ , with Stage 1 allowing aerosol particles greater than 0.8  $\mu\text{m}$ , and Stage 2 allowing aerosol particles with diameters less than 0.8  $\mu\text{m}$ . The bottom three stages of the Six-Stage sampler collected aerosols in diameters of 1.1–2.1  $\mu\text{m}$  (Stage 5), 0.65–1.1  $\mu\text{m}$  (Stage 6), and 0.65  $\mu\text{m}$  > D (Stage 7). One-stage and Six-Stage air samplers operated throughout the entirety of the AEROSE campaign. The air sampling flow rate was 2 L per minute over a 24-, 48-, or 72-h sampling period, depending on the sampling date. Glass fiber filters had very high retention of fine particles, with retention efficiency of 97–99% for 0.3  $\mu\text{m}$  particles. After sampling, filter samples were stored in air-tight plastic containers and analyzed for elemental composition. As shown in Figure 2, aerosol sampling primarily occurred in regions of high aerosol optical depth (AOD), according to time-averaged MODIS satellite retrievals (20 November 2015–10 December 2015).

### 2.2.2. Isotope Analysis of Dust Samples

Inductively Coupled Plasma Mass Spectrometry (ICP-MS) analysis detected metal isotope concentrations in dust-impacted AEROSE filter samples. Samples were analyzed using a PerkinElmer NexION 300D single quadrupole mass spectrometer coupled with ICP ionization. Detectable isotopes measured during this study included Al (isotope: 27), Ca (isotopes: 42, 43, 44, 46, 48), K (isotope: 39), Na (isotope: 23), Mg (isotopes: 24, 25, 26), Fe (isotopes: 54, 56, 57, 58), Ti (isotopes: 46, 47, 48, 49, 50), and Sr (isotopes: 84, 86, 87, 88). For ICP-MS sample preparation,  $\frac{1}{4}$  of each filter was digested in 20% nitric acid solution with ultrapure (18 M $\Omega$ m) water. The supernatant liquid was extracted from the filter samples and introduced to the ICP-MS, where the resulting plasma-induced ions could be separated and detected by the coupled mass spectrometer in terms of pulse intensity, measured in counts per second (cps). An external calibration standard (PerkinElmer's Instrument Calibration Standard 2) was used to convert ICP-MS intensity to sample concentration in parts per million (ppm). Calibration curves featured standard concentrations of 0.01, 0.05, 0.1, 0.5, and 1 ppm of each elemental isotope of interest to this investigation and were verified for linear correlations ( $R^2 > 0.9$ ). The internal standard (IS) set used for calibration quality included Be-9, In-115, U-238, CeO-156, Ce-140 (IS), Ce<sup>++</sup>70, with background 220 counts (cps) remaining below 1. Relative standard deviations (RSDs) were less than 5% for Ce-140 during preceding system performance checks. These internal standards resulted in elemental isotope intensity RSDs of less than 10% for all evaluated isotopes and below 5% for most.

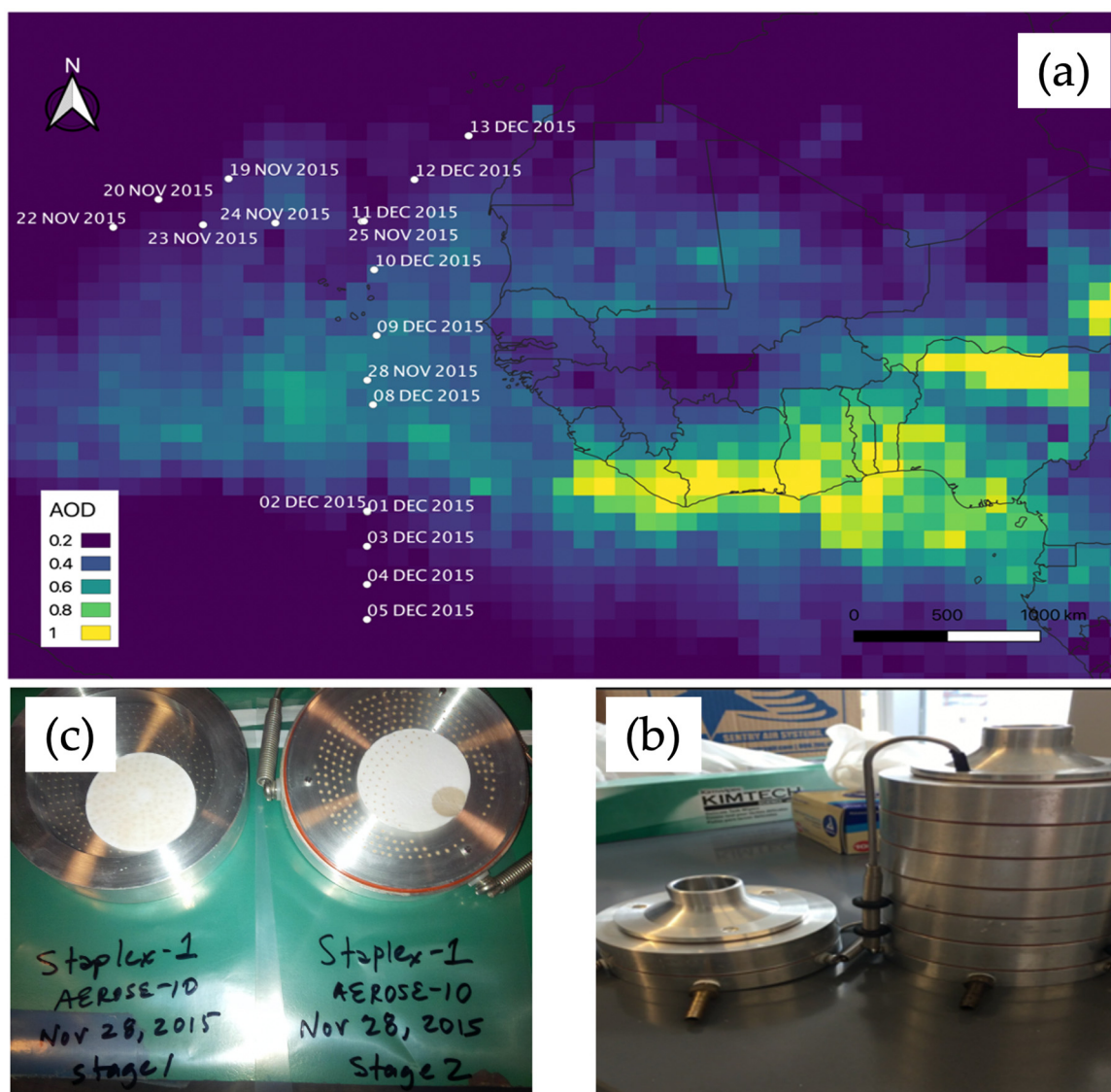


**Figure 2.** (a) Time-averaged MODIS Combined Dark Target and Deep Blue AOD retrieval at 0.55 microns for land and ocean; 1-degree daily AOD was averaged from 20 November 2015 to 10 December 2015 (b) One-Stage and Six-Stage cascade impactors deployed during the AEROSE campaign, (c) Dusty AEROSE '15 filter samples collected on 28 November 2015 using a One-Stage cascade impactator.

Dusty filter isotope concentrations were differenced by mean concentrations of environmental blank filters from the campaign to isolate dust aerosol contributions to measured isotopes. This method mitigated potential signal interference due to blank filter content and non-dust aerosol components. Ship-based sun photometer and interferometer measurements (to be discussed in Section 2.3.1), as well as Al concentration thresholds, were used to distinguish airmasses for environmental blank filter selections. During elemental analysis, non-Al isotope concentrations were divided by Al concentrations to normalize elemental data to an indicator of aluminosilicates present in Saharan dust.

The uncertainty in elemental ratios was quantified using error propagation principles to evaluate the limits of detection for isotopes of interest. Non-Al to Al isotope ratio uncertainty was quantified as

$$\Delta U = \sqrt{\left(\frac{\Delta E_{non-Al, blank}}{E_{non-Al, sample}}\right)^2 + \left(\frac{\Delta E_{Al, blank}}{E_{Al, sample}}\right)^2}, \quad (1)$$

where  $E$  and  $\Delta E$  represent the isotope concentration in dusty filters and the standard deviation of isotope concentration in blank filters, respectively. The first and second terms in the quadrature represent the fractional uncertainties in non-Al and Al isotope filter concentrations, respectively.

### 2.3. Source Region Identification of Dust Samples

#### 2.3.1. Dust Event Classification

Aerosol collection periods were labeled as distinctive dust events to compare source regions of AEROSE dust samples. Dust event designations were determined by relative maximums in dust aerosol presence, as determined by dust sample Al concentrations and ship-based radiometric aerosol retrievals. Aluminum concentration has been demonstrated to be a strong indicator of Saharan dust PM due to its aluminosilicate mineralogy [33,34].

For this study, the Marine Atmospheric Emitted Radiance Interferometer (M-AERI) was used for spectral detection of Saharan dust plumes throughout AEROSE '15. The M-AERI was operational from 17 November 2015 through 6 December 2015. This sea-going Fourier transform infrared (FTIR) spectrometer measured high-resolution infrared (IR) radiances from upward and downward viewing angles in nearly 5-min intervals [35]. Based on M-AERI retrievals from earlier campaigns, two narrow spectral channels were used for dust detection, namely  $961\text{ cm}^{-1}$  and  $1231\text{ cm}^{-1}$  [36]. Both channels are relatively insensitive to water vapor and ozone, but the  $961\text{ cm}^{-1}$  has much higher sensitivity to mineral dust; thus, we can use the following simple equation for dust detection:

$$D(T_B) = \frac{T_B(961\text{ cm}^{-1}) - T_B(1231\text{ cm}^{-1})}{T_B(961\text{ cm}^{-1}) + T_B(1231\text{ cm}^{-1})}, \quad (2)$$

where  $T_B$  is the wavenumber-dependent brightness temperature. The resultant dust signal was resampled to 1-h resolution.

Microtops II handheld sun photometers provided daytime, multi-channel, aerosol optical depth (AOD) measurements from the visible to the near-infrared spectrum of atmospheric columns during sun-viewing opportunities. These measurements were a part of NASA's Aerosol Robotic Network-Marine Aerosol Network (AERONET-MAN) observation system that provides satellite and aerosol transport model validation [37]. Sun photometer measurements were acquired in the 440, 500, 675, 870, and 936 nm solar spectrum bands during AEROSE '15. Level 2.0 AOD series datasets were used throughout this investigation.

If Al-26 concentrations, a proxy for dust particulate mass, exceeded 1 ppm (according to filter sample analysis) during elevated sun photometer aerosol optical depth (AOD) retrievals ( $>0.3$ ) or 90th percentile M-AERI dust retrievals, the dust sampling periods were considered Dense Events (DEs). The remaining sampling periods with detectable Al-26 concentrations above background concentrations were classified as Trace Events (TEs).

#### 2.3.2. Source Region Quantification

Statistical air-trajectory approaches, such as Potential Source Contribution Function (PSCF) and Concentration Weighted Trajectory (CWT), have been used to identify air pollutant sources [38–41]. These approaches quantify back-trajectory intersections with geospatial grid points, where PSCF uses background pollutant criteria to compute precursor back-trajectories probability and CWT uses grid trajectory residence time as a concentration weighting factor. PSCF, which is most applicable to isotope tracing, requires enough ambient pollutant concentrations associated with back-trajectories to mitigate high biases in PSCF values [38,40]. Due to PSCF limitations, AEROSE ship movement, and the 4-week duration of the campaign, this study used a novel approach for back-trajectory analysis that combines back trajectory grid densities and co-located satellite aerosol retrievals.

This study leveraged Hybrid Single Particle Lagrangian Integrated Trajectory (HYSPPLIT) trajectory models [42] and Visible Infrared Imaging Radiometer Suite (VIIRS) Level 3 (L3) satellite AOD retrievals [43] to quantify PSA contributions to AEROSE dust sample

PM. Dust event criteria (Section 2.3.1) were used to down-select back-trajectory periods that localize dust emission sources. PSA activity was quantified for each AEROSE '15 dust event using a potential source area frequency (PSAF) metric, where the weighted back-trajectory density per filter sample period was calculated. For this metric, we assimilate HYSPLIT back-trajectory and VIIRS aerosol optical depth data in  $1 \times 1$ -degree raster datasets for each dust event. The PSAF is calculated as

$$PSAF(d, h) = \frac{1}{n} \sum_{d=1}^n \tau(d) \times \sum_{h=1}^{120} I(h), \quad (3)$$

where  $\tau$  is VIIRS level-3 aerosol optical depth at appropriate 1-day intervals,  $d$ , and  $I$  is HYSPLIT intersections with VIIRS pixels at 1-h,  $h$ , initializations from sampling location. Then, 120-h HYSPLIT back-trajectories were simulated at 5 m above sea level (m a.s.l.) and initialized in hourly increments from the ship location during dusty observation periods. VIIRS AOD was temporally averaged from the dust sampling date to the date of the HYSPLIT intersection with the farthest PSA, totaling  $n$  number of days for averaging. In total, 5 m a.s.l. was determined to be representative of mean dust aerosol transport pathways within the atmospheric boundary layer based on comparisons to upper altitude back-trajectories (Figure S1, Supplemental Materials). Global Data Assimilation System (GDAS) data were used to compute back-trajectories.

For this study, the co-location and weighting of back-trajectory analysis with satellite AOD offer several advantages: (1) The hourly resolution of back-trajectories provides a statistically significant and representative sample size for reliable dust source identification of air sampler measurements, (2) By incorporating AOD, we can relate these back-trajectories to indicators of emission intensity per pixel, whereas traditional approaches use event probabilities per pixel, (3) We can quantify relative source contributions of dust events using fewer back-trajectories than traditionally required, (4) We are able to quantify relative source contributions using a consistent spatial framework of reference.

#### 2.4. Correlating Source Region Contributions to Elemental Isotope Ratios

The relationship between dust sample composition and PSA activity was evaluated using Pearson correlation metrics. We define PSAs for elemental discrimination according to prior Sahara Desert classifications [28,29], as shown in Figure 1. However, substantial dust emissions can occur between PSAs 2 and 3 in the El Djouf desert region [44], so this study created an additional PSA called PSA-2.5, also shown in Figure 1. For each PSA, this study evaluated the correlation ( $R^2$ ) between its mean PSAF values and elemental isotope ratios, where each AEROSE dust event was an independent observation in the analysis. In this study, we define very strong, strong, and moderate Pearson correlational strength as 0.8–1.0, 0.6–0.79, and 0.4–0.59, respectively.

### 3. Results and Discussion

#### 3.1. Source Region Identification

##### 3.1.1. Dust Event Detection and Classification

Corroborated AEROSE in situ observations revealed three dense and two trace dust events during the AEROSE '15 campaign. M-AERI dust signals, which ranged from roughly 0.3–0.4, reached the 90th percentile during the 11/20–11/22, 11/26, and 11/27 timeframes, and as high as the 80th percentile after 11/27, as shown by Figure 3

Concurrent sun photometer measurements peaked in AOD on 11/20 (0.33), 11/22 (0.51), 11/28 (0.45), and 12/09 (0.44), while the remaining measurement dates recorded AOD < 0.3. Al concentrations in filter samples exceeded 1 ppm during the 11/21–11/23, 11/26, 11/28, 12/03, and 12/09 collection dates, as shown in Figure 1. Lesser amounts of Al (1 ppm<) were observed on 11/27 and 12/09. Based on these observations and ship maneuver, we classify filter samples collected on 11/21–11/23, 11/25–11/26, 11/27, 11/28, and 12/09 as DE1, DE2, TE1, DE3, and TE2, respectively. The corroboration of cascade impactor

filter samples, sun-photometer, and M-AERI aerosol retrievals confirmed Saharan dust aerosol deposition within the marine boundary layer during the AEROSE '15 campaign.

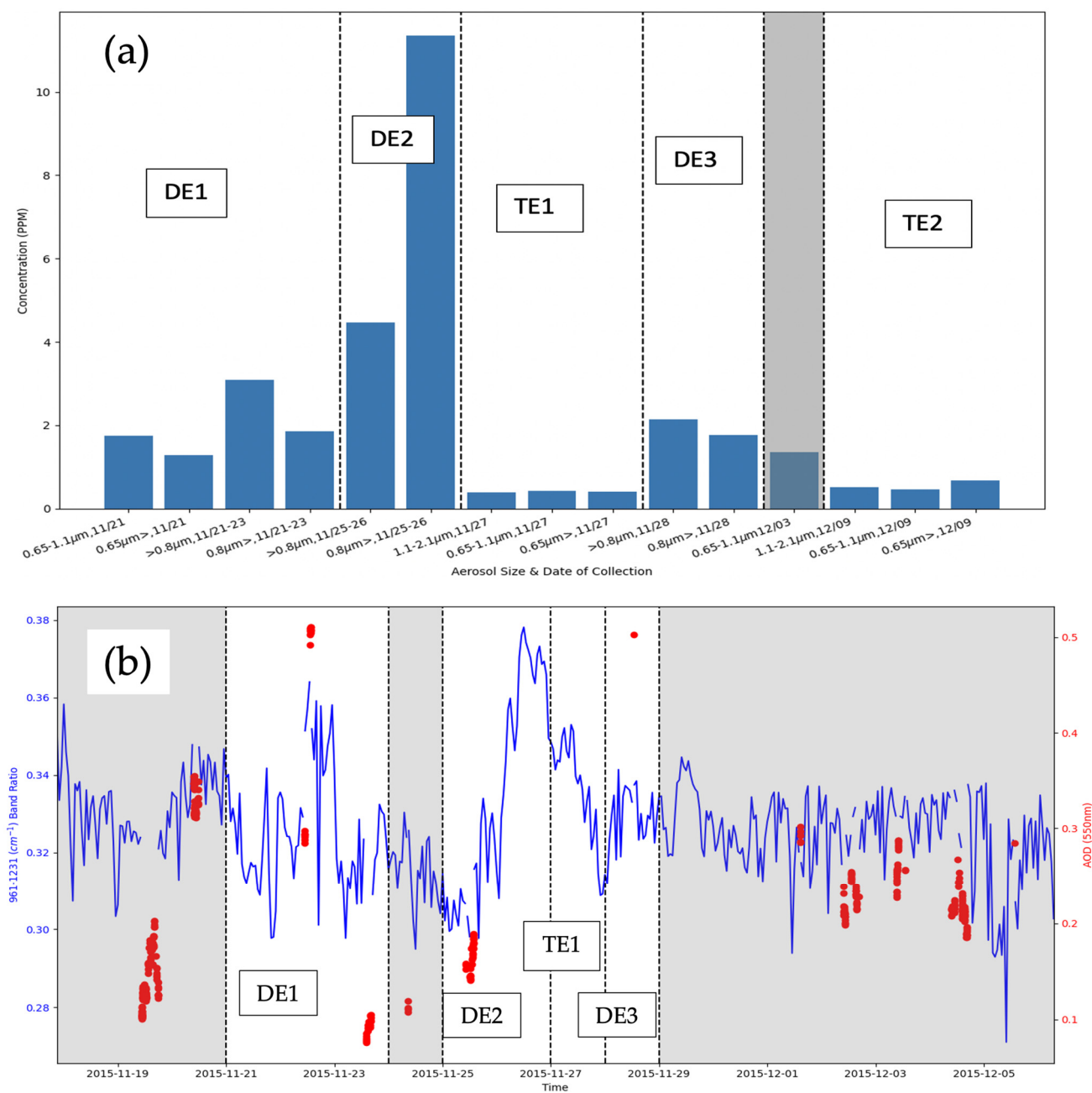


**Figure 3.** (a) Dust filter Al-27 concentration (ppm) collected during Cascade Impactor aerosol sampling and detected with ICP-MS. (b) Dust signal band ratios from M-AERI retrieval (blue) and AOD from ship-based sun-photometer measurements (red).

### 3.1.2. Source Region Quantification

PSAF analysis showed that a mixture of Saharan source regions (mostly PSA-2, PSA-2.5, and PSA-3) along a shared northeasterly wind trajectory likely contributed to high AOD observation periods in the Atlantic during AEROSE '15. Changes in these trajectories are closely associated with fluctuations in Harmattan pulses, determined by North African high-pressure and monsoonal tropical low-pressure orientations [33]. The majority of dust particulate sampled during AEROSE '15 likely originated in the western half of the Sahara Desert, with most emissions occurring outside previously established PSAs (PSA-2.5), as

shown in Figure 4 and Table 1. The El Djouf Desert, which resides in PSA-2.5, was the largest single contributor of dust aerosols sampled during the campaign, according to PSAF analysis. These findings exclude the Bodélé Depression as a likely source, which showed high levels of AOT near its source region, according to MODIS satellite imagery shown in Figure 2. Consistent with previous studies [25,44], this work demonstrates that established western Saharan PSAs must be geographically refined to accurately account for dust emissions in the tropical Atlantic.

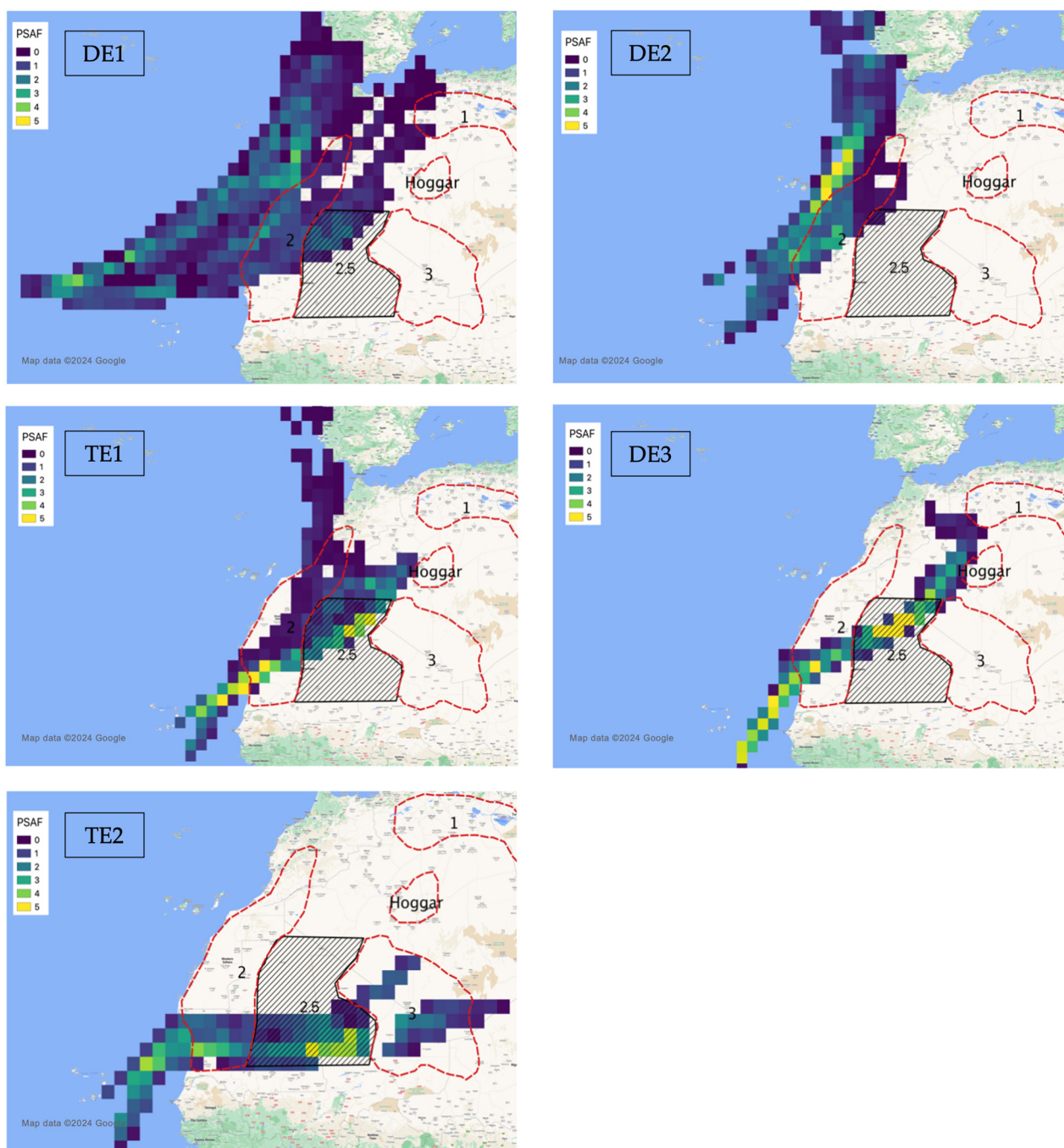


**Figure 4.** PSAF values for dust event DE1 (top left), DE2 (top right), TE1 (middle left), DE3 (middle right), and TE2 (bottom left) during the AEROSE '15 campaign. The color map represents PSAF frequency on a scale of 0 to 5 (purple to yellow). Red outlines represent PSA-1, PSA-2, PSA-3, and PSA-Hoggar. The additional PSA-2.5 is also shown in black shading. Map data were provided by ©2024 Google.

**Table 1.** The spatial mean of PSAF values within each PSA boundary was computed for each dust event during AEROSE '15.

Dust Events	Mean PSAF for PSA-1	Mean PSAF for PSA-2	Mean PSAF for PSA-2.5	Mean PSAF for PSA-3	Mean PSAF for PSA-Hoggar
DE1	0.089	0.932	1.096	0	0
DE2	0	1.206	0.276	0	0
DE3	0.006	0.487	0.810	0.003	0
TE1	0	0.959	1.875	2.435	0.610
TE2	0	1.601	1.859	1.123	0

This study finds that DE2 was the only AEROSE '15 dust episode with one primary source region, where PSA-2 contributed as much as 80% of the total PSAF for DE2. For the remainder of dust events, two or more PSAs each accounted for at least 33% of total PSAFs per dust event. PSA-2, the westernmost PSA, showed the second-highest PSAF; its most significant increases occurred during DE2 and TE2 (1.2 and 1.6, respectively). PSA-2.5, spanning eastern Mauritania and Western Mali, was the most active of PSAs with the highest dust contributions occurring during TE1 and TE2 (PSAF > 1.8). PSA-3, bordering southwestern Algeria and eastern Mali, demonstrated moderate activity levels throughout the campaign; its highest PSAF was during TE1 and TE2 sampling periods (2.4 and 1.1, respectively).

### 3.2. Elemental Characterizations of AEROSE '15 Dust Samples

#### 3.2.1. Dust Event Isotope Concentrations

Elemental isotope concentrations in AEROSE '15 dust samples were spatially and temporally dynamic over the 4-week sampling period, according to ICP-MS analysis. We observe that each AEROSE '15 dust event had a unique elemental isotope signature, as shown in Figure 5. This variability in isotope concentration was indicative of changes in Saharan source region contributions and atmospheric processing of mineral dust. Ca, Fe, K, Mg, Sr, and Ti isotope ratios (per Al-26) were particularly useful discriminators of airmass and source region changes throughout AEROSE '15 aerosol sampling periods. In various combinations, these isotope ratios reached local maximums during DE2, TE1, and TE2. These elemental isotope signals highlight the chemical complexity of Saharan dust plumes that is often undetectable from satellite observations.

Ca-44 per Al-27 ratios ranged between 0.8 and 1.7 during the AEROSE '15 campaign. The mean and standard deviation for dusty filters was 1.11 and 0.26, respectively. Peak ratios occurred during DE2 and TE2 with values of 1.72 (1.28) and 1.39 (1.21) in the largest (finest) size fraction. Ca/Al ratios were highest in the coarsest size fraction for all dust events except TDE2, where peak concentrations occurred in the 0.65–1.1  $\mu\text{m}$  range. Many studies have confined size-dependency trends in Ca concentrations to Moroccan and Saudi Arabian desert soils [14,33,45,46], which is consistent with our observations.

Fe-57 per Al ratios ranged between 0 and 0.4 during dust event observation periods for the campaign. The mean and standard deviations for all dusty filters were 0.22 and 0.10, respectively. The TE1 sampling period recorded the highest Fe-57 ratios, at roughly 0.4. In contrast to Ca/Al ratios, this study did not observe significant size dependencies in measured Fe-57 ratios.

K-39 per Al ratios ranged between 0.2 and 0.5 throughout the campaign; the mean and standard deviations were 0.28 and 0.08, respectively. Peak K-39 ratios (0.3–0.5) were observed during TE1 and TE2 sampling periods.

Mg-24 per Al ratios were relatively stable at 0.2 to 0.4, with peak ratios occurring during the DE2 observation period. The mean and standard deviations were 0.36 and 0.07, respectively.

This study observed highly correlated Ti-48 and Sr-88 ratios (per Al) throughout the campaign that fell within the range of 0.02–0.3. For Ti-48, the mean and standard deviations were 0.09 and 0.08, respectively. For Sr-88, the mean and standard deviations were 0.06 and 0.09, respectively. Ti-48 and Sr-88 peaked in concentration ratios, measured near 0.3, during the TE1 sampling period.

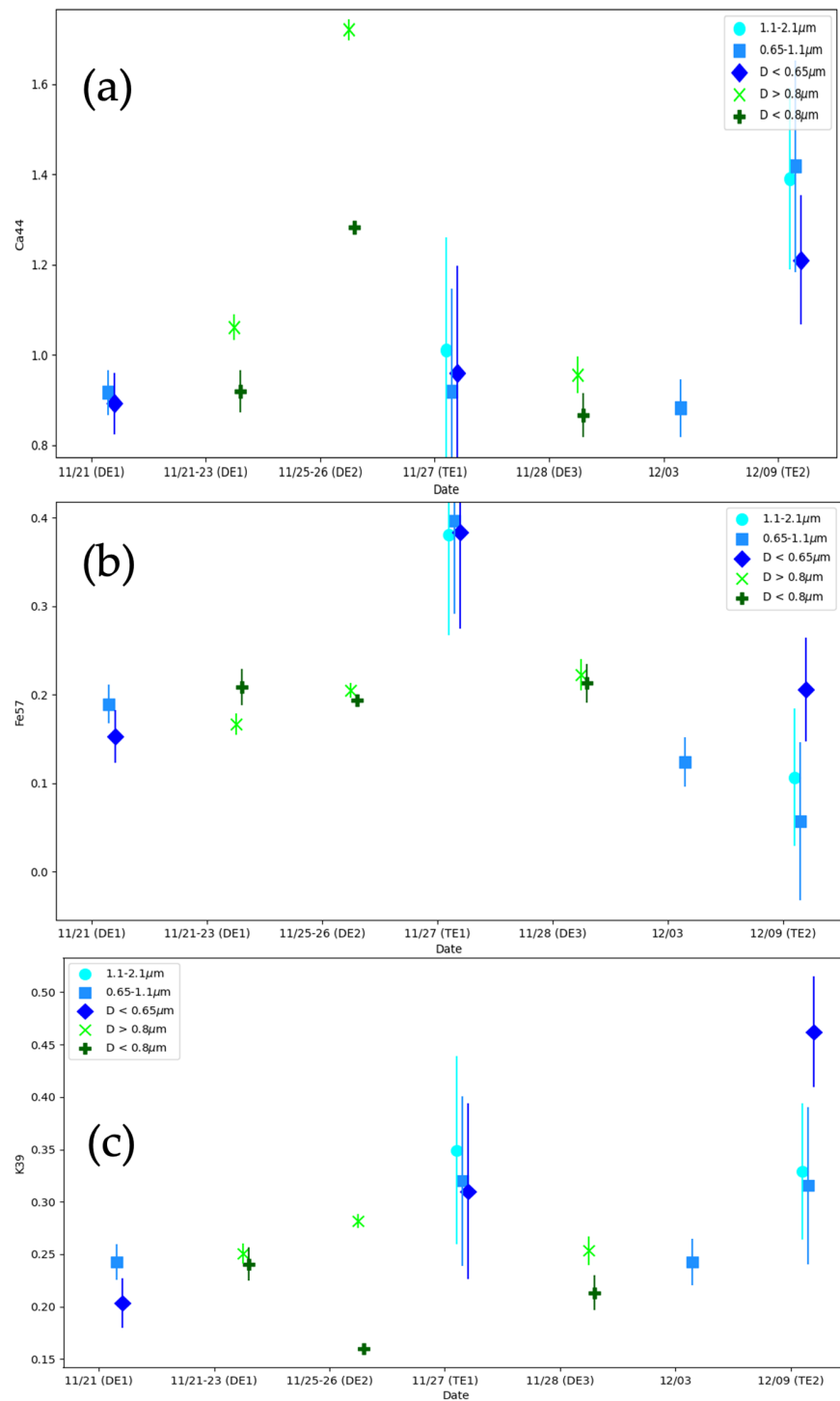
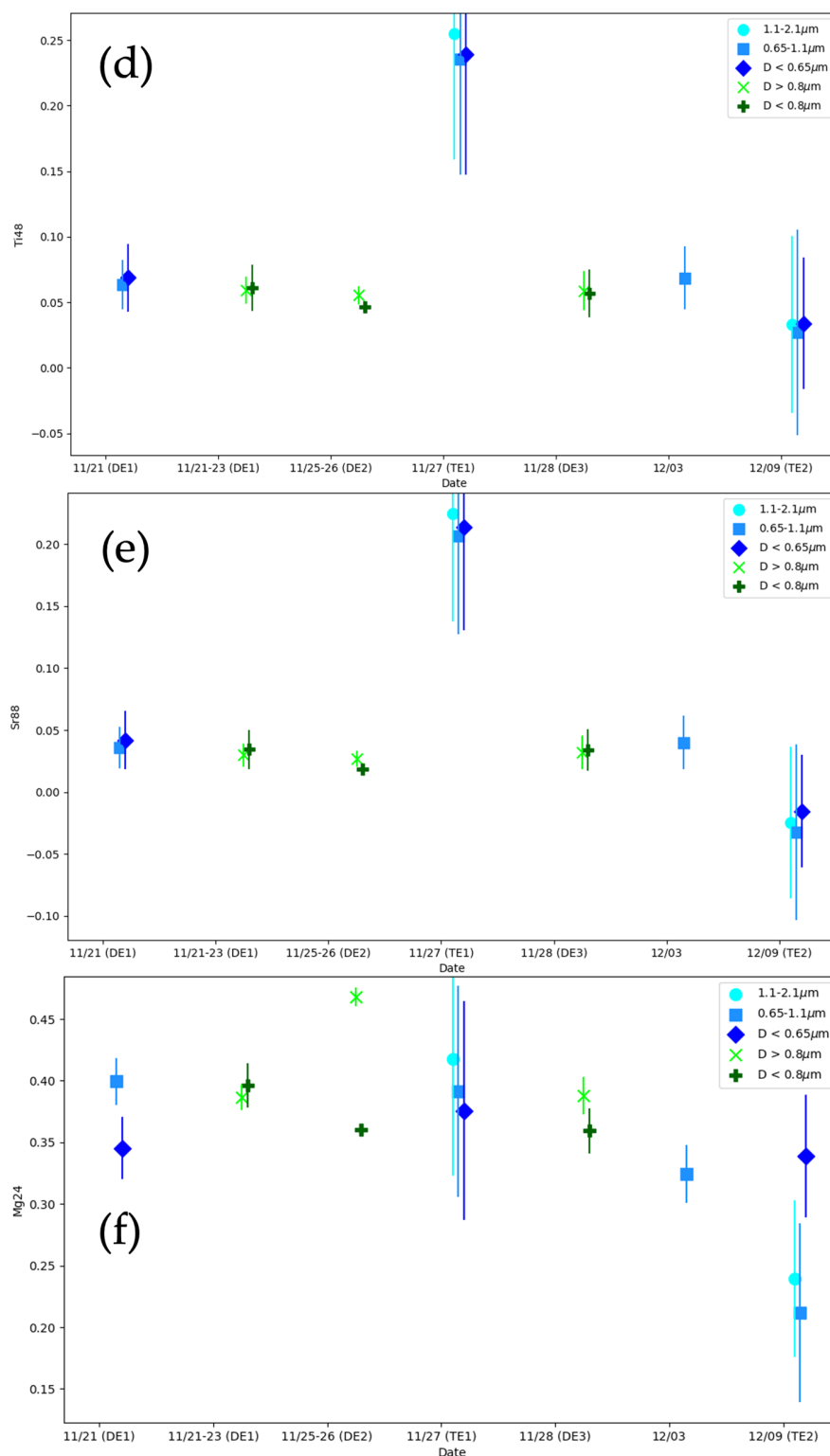


Figure 5. Cont.



**Figure 5.** ICP-MS elemental isotope concentration ratios per Al-26 for aerosol filter samples collected during AEROSE '15 dust events. Ca-44 (a), Fe-57 (b), K-39 (c), Ti-48 (d), Sr-88 (e), and Mg-24 (f) ratios are shown per time with associated dust events labeled in parenthesis. Each aerosol size fraction was plotted and illustrated per observation period using a respective symbology and color coding. Filter sample elemental ratios for six-stage and two-stage samplers are shown in blue and green, respectively. Circles, squares, diamonds, exes, and pluses represent 1.1–2.1  $\mu\text{m}$  (Stage 5), 0.65–1.1  $\mu\text{m}$  (Stage 6),  $0.65 \mu\text{m} > D$ ,  $D > 0.8 \mu\text{m}$ , and  $D < 0.8 \mu\text{m}$  aerosol diameters, respectively. Uncertainty bars for each elemental isotope ratio are shown across all AEROSE '15 observation periods.

### 3.2.2. Correlational Analysis of Dust Sample Isotopes and Source Region Emissions

Pearson correlational analysis identified statistical relationships between elemental isotope ratios and PSA apportionments of AEROSE '15 dust events. Each attributed PSA demonstrated significant correlations with specific elemental isotopes measured in this study, as shown in Figure 6. Collectively, these isotope correlations produced unique spectral signatures of each North African PSA sampled during the campaign.

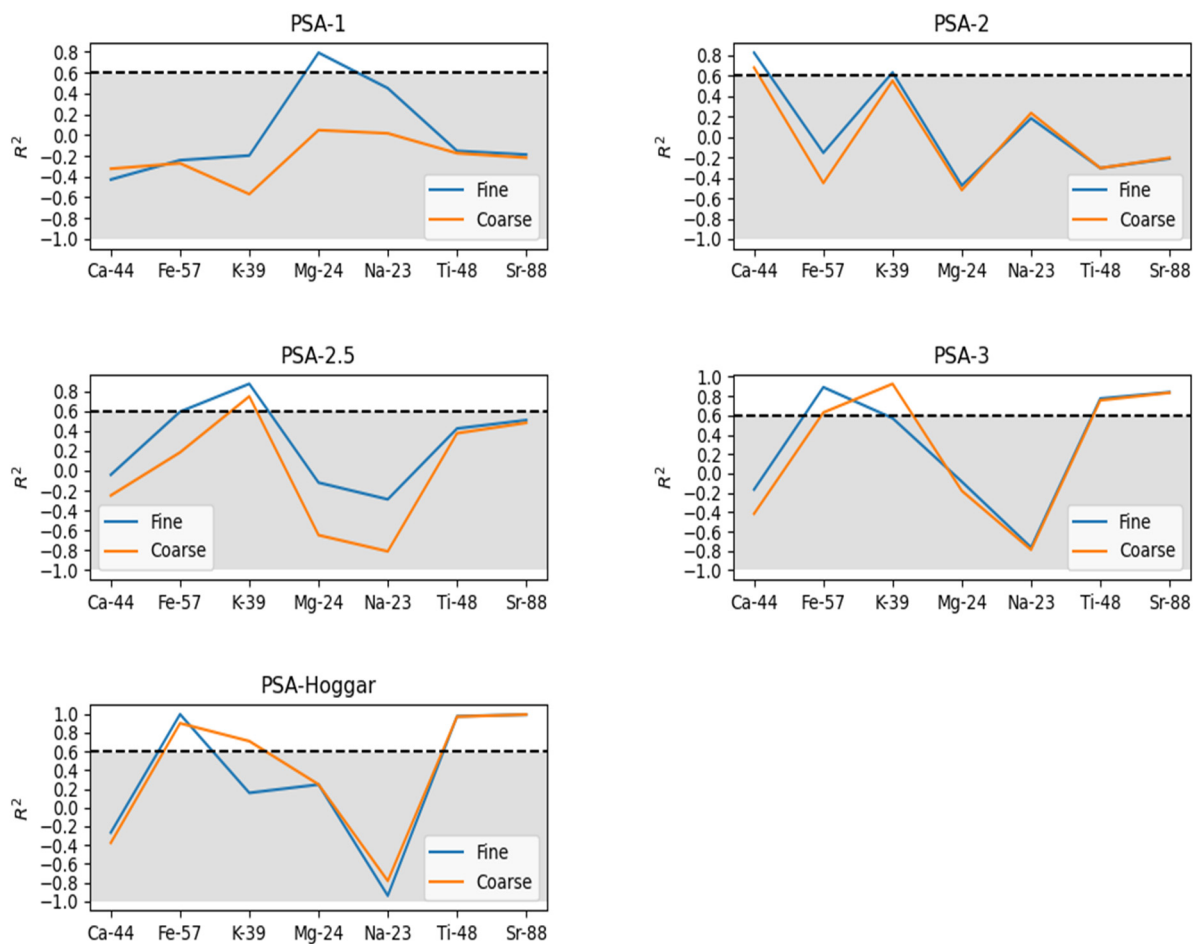


**Figure 6.** Pearson correlation between dust filter isotope ratios (discussed in Section 3.2.1) and mean PSAF (Table 1) for each source region; the area above the dashed line represents strong to very strong correlations ( $R^2 > 0.59$  and  $R^2 > 0.79$ ). Each PSA-isotope correlation is shown individually (PSA1: **top left**, PSA-2: **top right**, PSA-2.5: **middle left**, PSA-3: **middle right**, PSA-Hoggar: **bottom left**). Fine and coarse fraction (at  $0.8 \mu\text{m}$ ) dust sample correlations are shown in blue and orange, respectively. The corresponding  $p$ -values for highly correlated isotopes and PSAs ( $R^2 > 0.79$ ) were: Ca-44 and PSA-2: 0.08 (fine); K-39 and PSA-2.5: 0.05 (fine); Mg-24 and PSA-1: 0.11 (fine); Fe-47 and PSA-3: 0.04 (fine); Fe-47 and Hoggar: 0.04 (coarse) and 0.009 (fine); Ti-48 and PSA-3: 0.08 (coarse) and 0.08 (fine); Ti-48 and Hoggar: 0.001 (coarse) and 0.001 (fine); Sr-88 and PSA-3: 0.14 (coarse) and 0.12 (fine); Sr-88 and Hoggar: 0.01 (coarse) and 0.01 (fine).

PSA-2 dust emissions were very strongly and strongly correlated with Ca-44 and K-39 isotope ratios, respectively.  $R^2$  values for Ca-44 and PSA-2 were near 0.8 and 0.7 for fine and coarse dust aerosol fractions, respectively. K-39 and PSA-2 correlational values were near 0.6 for both fine- and coarse-sized sample fractions. The very strong correlation between Ca-44 ratios and PSA-2 emissions was consistent with several literature findings demonstrating elevated calcium content in Moroccan, Western Saharan, and Mauritanian soils [14,33,46]. Ephemeral lakes containing calcite minerals are a likely source of Ca isotopes measured from PSA-2 [7,45]. However, studies have also linked

anthropogenic sources in Morocco and Western Sahara to higher Ca content in downwind mineral dust [7,26]. Mining activities related to rock extraction, wind erosion of exposed mining sites, changes in soil texture, and phosphoric acid production can influence dust aerosol emissions in the region. Additionally, agricultural fields in western Marrakesh have been linked to dust emissions [7]. This study identified a region near the port city of El Marsa, Western Sahara, as the most likely anthropogenic source (nearest PSAF pixel > 5) of high Ca-44 ratios during DE2 ( $\text{Ca}/\text{Al} > 1.7$ ); this site exports phosphorous rock from the nearby Bou Craa phosphorous mining facility using a 100 km conveyor belt. The geochemical composition of these sedimentary phosphate rock deposits is primarily CaO and  $\text{P}_2\text{O}_5$  oxides [47], which is often detectable in Ca/Al ratios (in addition to P, Cl, nitrates, sulfates, and ammonium) in mineral dust at receptor sites downwind of Moroccan mining facilities [26]. Based on this analysis, Ca isotope ratios are a strong indicator of PSA-2 dust aerosol emissions due to natural and anthropogenic sources near ephemeral lakes, mining facilities, and agricultural sites.

PSA-2.5 dust emissions were very strongly correlated with K-39 ratios and moderately correlated with fine fraction Fe-57 ratios. Previous studies have linked high K/Al ratios with the presence of illite clay minerals in Saharan soils [33,48]. The illite mass fraction in clay minerals has been shown to exceed 40% in Mauritania and 30% in much of the El Djouf Desert, according to mineral mapping and characterization efforts [14,45]. Thus, the high correlation we observe between K-39 ratios and PSA-2.5 emissions may be an indicator of K-bearing illite minerals found in high abundance near the El Djouf Desert. This elemental indicator could benefit model validation studies and satellite observations constraining PSA-2.5 emissions, an underpredicted source region of Saharan dust export to the Atlantic [25,44]. The activity and elemental distinctiveness of PSA-2.5 dust emissions also highlight the need for refinement of traditional PSA designations in the Sahara to improve desert aerosol flux estimates.

PSA-3 dust emissions were very strongly correlated with fine fraction Fe-57 and Ti-48 ratios, and strongly correlated with Sr-88 and coarse fraction Fe-57 ratios. The abundance of Fe-57 in PSA-3 is consistent with prior studies evaluating Fe/Al ratios in PSA-3 [33]. The strong correlation between Fe-57 ratios and PSA-3 emissions is likely associated with the abundance of iron-rich, hematite and goethite minerals (greater than 3% in clay soils) within the PSA-3 boundary [14]. Additionally, the correlation of Ti-48 and Fe-57 ratios in PSA-3 relates to previous studies that have identified titanium oxide and iron oxide minerals in Sahelian soils [15].

PSA-1 and PSA-Hoggar exhibited low dust emissions in this study, limiting analytical judgements on source elemental indicators. However, the high correlations between Mg ratios and PSA-1 that we observe have been shown to be an indicator of dolomite minerals present in northern Algeria, based on previous chemical analysis of Saharan dust aerosols sampled at the Canary Islands [33].

#### 4. Conclusions

In summary, cascade impactor air sampler size-dependently collected airborne Saharan dust particulate matter in the tropical Atlantic during the 2015 AEROSE campaign. ICP-MS analysis measured elemental isotope concentrations in dust-impacted air sampler filters from the 4-week campaign. The probable source regions of these isotopes were determined using a newly defined air back-trajectory method and PSA correlational analysis. The results of this study show that:

- Regionally specific elemental indicators remain detectable in dust aerosols collected along the Saharan air layer trajectory far into the Tropical Atlantic marine boundary layer. We find that the combination of Ca, Fe, K, Sr, and Ti isotopes can uniquely fingerprint PSA contributions in downwind Saharan dust particulates sampled in the tropical Atlantic. These elemental characteristics can change rapidly over sub-weekly timescales and short distances (1000 km $>$ ) within the tropical Atlantic.

- Western Sahara (PSA-2) was the largest contributor of Ca isotopes detected during AEROSE dust observation periods; previous studies have traced Ca-rich dust aerosols to the northern latitudes of Morocco and Algeria [29,33]. The very strong correlation ( $R$ -squared  $> 0.79$ ) between Ca-44 and PSA-2 dust emissions was attributed to calcite minerals from dry lake beds and mining activities in Western Sahara.
- K-39 isotopes were very strongly correlated with El Djouf Desert aerosol emissions (PSA-2.5). The correlation between K-39 ratios and PSA-2.5 was a likely indicator of illite minerals near the El Djouf Desert region, according to corroboration with mineral mapping studies. Previous studies have shown that this region could be the second largest dust aerosol emitter in the Sahara, despite its non-attribution in previous PSA designations [25,44].
- PSA-3 dust emissions were very strongly correlated with Fe, Ti, and Sr isotopes. Fe-57 isotope correlations may indicate that iron oxide mineral deposition is occurring at a higher rate following PSA-3 dust emissions; these minerals may have important implications for oceanic carbon cycling since they are limiting nutrients in marine ecosystem productivity.

The geochemical tracers identified in AEROSE dust samples can support climate model estimates and satellite retrievals of Saharan aerosol source region emissions, deposition rates, and radiative effects. These estimates vary significantly due to unresolved model parameterizations of dust microphysical properties, source region apportionment, and model ensemble variability [3,7,49,50]. Size-resolved elemental characterizations of mineral dust can improve refractive index parameterizations in dust aerosol models, a key uncertainty in dust radiative effects. Additionally, the geochemical tracers identified in this study can address source region apportionment uncertainties in dust model simulations. We anticipate that the multi-decadal record of AEROSE measurements in the tropical Atlantic will support the advancement of regional aerosol observational networks for dust model validation and satellite retrieval.

**Supplementary Materials:** The following supporting information can be downloaded at: <https://www.mdpi.com/article/10.3390/atmos15050554/s1>, Figure S1: Back-Trajectory Height Analysis.

**Author Contributions:** Conceptualization, D.E.Y. and V.R.M.; methodology, D.E.Y.; validation, D.E.Y. and V.R.M.; formal analysis, D.E.Y.; investigation, D.E.Y. and V.R.M.; resources, D.E.Y. and V.R.M.; writing—original draft preparation, D.E.Y.; writing—review and editing, D.E.Y. and V.R.M.; visualization, D.E.Y.; funding acquisition, V.R.M. All authors have read and agreed to the published version of the manuscript.

**Funding:** This work was funded by the NOAA Cooperative Science Center in Atmospheric Sciences and Meteorology (NCAS-M) under the NOAA Educational Partnership Program Cooperative Agreement #NA16SEC4810006.

**Institutional Review Board Statement:** Not applicable.

**Informed Consent Statement:** Not applicable.

**Data Availability Statement:** The raw data supporting the conclusions of this article will be made available by the authors on request. The data are not publicly available due to privacy.

**Acknowledgments:** We would like to thank the AEROSE and PNE science team members, as well as NATO Alliance crew, for their continuous environmental data collection efforts at sea. Dust elemental analysis was performed at the University of Maryland Baltimore County (UMBC) Molecular Characterization and Analysis Complex (MCAC). We acknowledge the NOAA Air Resources Laboratory for HYSPLIT transport and dispersion model access. Satellite products were acquired from the Level-1 and Atmosphere Archive and Distribution System (LAADS) 435 Distributed Active Archive Center (DAAC), located at the Goddard Space Flight Center in Greenbelt, Maryland (<https://ladsweb.nascom.nasa.gov/>; accessed on 1 September 2023). We thank Nicholas Nalli for his technical review of the manuscript, NRV Alliance cruise data, and AERONET-MAN data contributions.

**Conflicts of Interest:** Author Daniel E. Yeager was employed by the company The Aerospace Corporation. The remaining authors declare that the research was conducted in the absence of any commercial or financial relationships that could be construed as a potential conflict of interest.

## References

1. Kaufman, Y.J.; Koren, I.; Remer, L.A.; Tanré, D.; Ginoux, P.; Fan, S. Dust Transport and Deposition Observed from the Terra-Moderate Resolution Imaging Spectroradiometer (MODIS) Spacecraft over the Atlantic Ocean. *J. Geophys. Res. D Atmos.* **2005**, *110*, 10–12. [[CrossRef](#)]
2. d’Almeida, G.A. A Model for Saharan Dust Transport. *J. Appl. Meteorol. Clim.* **1986**, *25*, 903–916. [[CrossRef](#)]
3. Kok, J.; Adebisi, A.; Albani, S.; Balkanski, Y.; Checa-Garcia, R.; Chin, M.; Colarco, P.; Hamilton, D.; Huang, Y.; Ito, A.; et al. Contribution of the World’s Main Dust Source Regions to the Global Cycle of Desert Dust. *Atmos. Chem. Phys.* **2021**, *21*, 8169–8193. [[CrossRef](#)]
4. Prospero, J.M.; Ginoux, P.; Torres, O.; Nicholson, S.E.; Gill, T.E. Environmental Characterization of Global Sources of Atmospheric Soil Dust Identified with the Nimbus 7 Total Ozone Mapping Spectrometer (TOMS) Absorbing Aerosol Product. *Rev. Geophys.* **2002**, *40*, 2-1-2–31. [[CrossRef](#)]
5. Washington, R.; Bouet, C.; Cautenet, G.; Mackenzie, E.; Ashpole, I.; Engelstaedter, S.; Lizcano, G.; Henderson, G.M.; Schepanski, K.; Tegen, I. Dust as a Tipping Element: The Bodélé Depression, Chad. *Proc. Natl. Acad. Sci. USA* **2009**, *106*, 20564. [[CrossRef](#)] [[PubMed](#)]
6. Ismail, S.; Ferrare, R.A.; Browell, E.V.; Kooi, S.A.; Dunion, J.P.; Heymsfield, G.; Notari, A.; Butler, C.F.; Burton, S.; Fenn, M.; et al. LASE Measurements of Water Vapor, Aerosol, and Cloud Distributions in Saharan Air Layers and Tropical Disturbances. *J. Atmos. Sci.* **2010**, *67*, 1026–1047. [[CrossRef](#)]
7. Ginoux, P.; Prospero, J.M.; Gill, T.E.; Hsu, N.C.; Zhao, M. Global-Scale Attribution of Anthropogenic and Natural Dust Sources and Their Emission Rates Based on MODIS Deep Blue Aerosol Products. *Rev. Geophys.* **2012**, *50*. [[CrossRef](#)]
8. Miller, R.L.; Knippertz, P.; Pérez García-Pando, C.; Perlwitz, J.P.; Tegen, I. Impact of Dust Radiative Forcing upon Climate. In *Mineral Dust: A Key Player in the Earth System*; Knippertz, P., Stuut, J.-B.W., Eds.; Springer Netherlands: Dordrecht, The Netherlands, 2014; pp. 327–357. ISBN 978-94-017-8978-3.
9. Flores, A.; Sakai, R.K.; Joseph, E.; Nalli, N.R.; Smirnov, A.; Demoz, B.; Morris, V.R.; Wolfe, D.; Chiao, S. On Saharan Air Layer Stability and Suppression of Convection over the Northern Tropical Atlantic: Case Study Analysis of a 2007 Dust Outflow Event. *Atmosphere* **2023**, *14*, 707. [[CrossRef](#)]
10. Hoose, C.; Möhler, O. Heterogeneous Ice Nucleation on Atmospheric Aerosols: A Review of Results from Laboratory Experiments. *Atmos. Chem. Phys.* **2012**, *12*, 9817–9854. [[CrossRef](#)]
11. Zhang, Y.; Mahowald, N.; Scanza, R.A.; Journet, E.; Desboeufs, K.; Albani, S.; Kok, J.F.; Zhuang, G.; Chen, Y.; Cohen, D.D.; et al. Modeling the Global Emission, Transport and Deposition of Trace Elements Associated with Mineral Dust. *Biogeosciences* **2015**, *12*, 5771–5792. [[CrossRef](#)]
12. Prospero, J.M.; Mayol-Bracero, O.L. Understanding the Transport and Impact of African Dust on the Caribbean Basin. *Bull. Am. Meteorol. Soc.* **2013**, *94*, 1329–1337. [[CrossRef](#)]
13. Garrison, V.H.; Majewski, M.S.; Konde, L.; Wolf, R.E.; Otto, R.D.; Tsuneoka, Y. Inhalable Desert Dust, Urban Emissions, and Potentially Biotoxic Metals in Urban Saharan-Sahelian Air. *Sci. Total Environ.* **2014**, *500–501*, 383–394. [[CrossRef](#)] [[PubMed](#)]
14. Journet, E.; Balkanski, Y.; Harrison, S.P. A New Data Set of Soil Mineralogy for Dust-Cycle Modeling. *Atmos. Chem. Phys.* **2014**, *14*, 3801–3816. [[CrossRef](#)]
15. Formenti, P.; Caquineau, S.; Desboeufs, K.; Klaver, A.; Chevaillier, S.; Journet, E.; Rajot, J.L. Mapping the Physico-Chemical Properties of Mineral Dust in Western Africa: Mineralogical Composition. *Atmos. Chem. Phys.* **2014**, *14*, 10663–10686. [[CrossRef](#)]
16. Kok, J.F. A Scaling Theory for the Size Distribution of Emitted Dust Aerosols Suggests Climate Models Underestimate the Size of the Global Dust Cycle. *Proc. Natl. Acad. Sci. USA* **2011**, *108*, 1016–1021. [[CrossRef](#)] [[PubMed](#)]
17. Kok, J.F.; Ridley, D.A.; Zhou, Q.; Miller, R.L.; Zhao, C.; Heald, C.L.; Ward, D.S.; Albani, S.; Haustein, K. Smaller Desert Dust Cooling Effect Estimated from Analysis of Dust Size and Abundance. *Nat. Geosci.* **2017**, *10*, 274–278. [[CrossRef](#)] [[PubMed](#)]
18. Di Biagio, C.; Boucher, H.; Caquineau, S.; Chevaillier, S.; Cuesta, J.; Formenti, P. Variability of the Infrared Complex Refractive Index of African Mineral Dust: Experimental Estimation and Implications for Radiative Transfer and Satellite Remote Sensing. *Atmos. Chem. Phys.* **2014**, *14*, 11093–11116. [[CrossRef](#)]
19. Castellanos, P.; Colarco, P.; Espinosa, W.R.; Guzewich, S.D.; Levy, R.C.; Miller, R.L.; Chin, M.; Kahn, R.A.; Kempainen, O.; Moosmüller, H.; et al. Mineral Dust Optical Properties for Remote Sensing and Global Modeling: A Review. *Remote Sens. Environ.* **2024**, *303*, 113982. [[CrossRef](#)]
20. Ravelo-Pérez, L.M.; Rodríguez, S.; Galindo, L.; García, M.I.; Alastuey, A.; López-Solano, J. Soluble Iron Dust Export in the High Altitude Saharan Air Layer. *Atmos. Environ.* **2016**, *133*, 49–59. [[CrossRef](#)]
21. de Baar, H.J.W.; Boyd, P.W.; Coale, K.H.; Landry, M.R.; Tsuda, A.; Assmy, P.; Bakker, D.C.E.; Bozec, Y.; Barber, R.T.; Brzezinski, M.A.; et al. Synthesis of Iron Fertilization Experiments: From the Iron Age in the Age of Enlightenment. *J. Geophys. Res. Ocean.* **2005**, *110*. [[CrossRef](#)]

22. Lapointe, B.E.; Brewton, R.A.; Herren, L.W.; Wang, M.; Hu, C.; McGillicuddy, D.J.; Lindell, S.; Hernandez, F.J.; Morton, P.L. Nutrient Content and Stoichiometry of Pelagic Sargassum Reflects Increasing Nitrogen Availability in the Atlantic Basin. *Nat. Commun.* **2021**, *12*, 3060. [[CrossRef](#)] [[PubMed](#)]
23. Bozlaker, A.; Prospero, J.M.; Fraser, M.P.; Chellam, S. Quantifying the Contribution of Long-Range Saharan Dust Transport on Particulate Matter Concentrations in Houston, Texas, Using Detailed Elemental Analysis. *Environ. Sci. Technol.* **2013**, *47*, 10179–10187. [[CrossRef](#)] [[PubMed](#)]
24. Gross, A.; Palchan, D.; Krom, M.D.; Angert, A. Elemental and Isotopic Composition of Surface Soils from Key Saharan Dust Sources. *Chem. Geol.* **2016**, *442*, 54–61. [[CrossRef](#)]
25. Guinoiseau, D.; Singh, S.P.; Galer, S.J.G.; Abouchami, W.; Bhattacharyya, R.; Kandler, K.; Bristow, C.; Andreae, M.O. Characterization of Saharan and Sahelian Dust Sources Based on Geochemical and Radiogenic Isotope Signatures. *Quat. Sci. Rev.* **2022**, *293*, 107729. [[CrossRef](#)]
26. Rodríguez, S.; Alastuey, A.; Alonso-Pérez, S.; Querol, X.; Cuevas, E.; Abreu-Afonso, J.; Viana, M.; Pérez, N.; Pandolfi, M.; De La Rosa, J. Transport of Desert Dust Mixed with North African Industrial Pollutants in the Subtropical Saharan Air Layer. *Atmos. Chem. Phys.* **2011**, *11*, 6663–6685. [[CrossRef](#)]
27. Querol, X.; Tobias, A.; Pérez, N.; Karanasiou, A.; Amato, F.; Stafoggia, M.; Pérez García-Pando, C.; Ginoux, P.; Forastiere, F.; Gummy, S.; et al. Monitoring the Impact of Desert Dust Outbreaks for Air Quality for Health Studies. *Environ. Int.* **2019**, *130*, 104867. [[CrossRef](#)] [[PubMed](#)]
28. Formenti, P.; Schütz, L.; Balkanski, Y.; Desboeufs, K.; Ebert, M.; Kandler, K.; Petzold, A.; Scheuven, D.; Weinbruch, S.; Zhang, D. Recent Progress in Understanding Physical and Chemical Properties of African and Asian Mineral Dust. *Atmos. Chem. Phys.* **2011**, *11*, 8231–8256. [[CrossRef](#)]
29. Scheuven, D.; Schütz, L.; Kandler, K.; Ebert, M.; Weinbruch, S. Bulk Composition of Northern African Dust and Its Source Sediments—A Compilation. *Earth Sci. Rev.* **2013**, *116*, 170–194. [[CrossRef](#)]
30. Morris, V.; Clemente-Colón, P.; Nalli, N.R.; Joseph, E.; Armstrong, R.A.; Detrés, Y.; Goldberg, M.D.; Minnett, P.J.; Lumpkin, R. Measuring Trans-Atlantic Aerosol Transport from Africa. *Eos. Trans. Am. Geophys. Union* **2006**, *87*, 565–571. [[CrossRef](#)]
31. Nalli, N.R.; Joseph, E.; Morris, V.R.; Barnet, C.D.; Wolf, W.W.; Wolfe, D.; Minnett, P.J.; Szczodrak, M.; Izaguirre, M.A.; Lumpkin, R.; et al. Multiyear Observations of the Tropical Atlantic Atmosphere: Multidisciplinary Applications of the NOAA Aerosols and Ocean Science Expeditions. *Bull. Am. Meteorol. Soc.* **2011**, *92*, 765–789. [[CrossRef](#)]
32. Bourlès, B.; Lumpkin, R.; McPhaden, M.J.; Hernandez, F.; Nobre, P.; Campos, E.; Yu, L.; Planton, S.; Busalacchi, A.; Moura, A.D.; et al. THE PIRATA PROGRAM: History, Accomplishments, and Future Directions. *Bull. Am. Meteorol. Soc.* **2008**, *89*, 1111–1126. [[CrossRef](#)]
33. Rodríguez, S.; Calzolari, G.; Chiari, M.; Nava, S.; García, M.I.; López-Solano, J.; Marrero, C.; López-Darias, J.; Cuevas, E.; Alonso-Pérez, S.; et al. Rapid Changes of Dust Geochemistry in the Saharan Air Layer Linked to Sources and Meteorology. *Atmos. Environ.* **2020**, *223*, 117186. [[CrossRef](#)]
34. Fitzgerald, E.; Ault, A.P.; Zauscher, M.D.; Mayol-Bracero, O.L.; Prather, K.A. Comparison of the Mixing State of Long-Range Transported Asian and African Mineral Dust. *Atmos. Environ.* **2015**, *115*, 19–25. [[CrossRef](#)]
35. Minnett, P.J.; Knuteson, R.O.; Best, F.A.; Osborne, B.J.; Hanafin, J.A.; Brown, O.B. The Marine-Atmospheric Emitted Radiance Interferometer: A High-Accuracy, Seagoing Infrared Spectroradiometer. *J. Atmos. Ocean Technol.* **2001**, *18*, 994–1013. [[CrossRef](#)]
36. Nalli, N.R.; Clemente-Colón, P.; Minnett, P.J.; Szczodrak, M.; Morris, V.; Joseph, E.; Goldberg, M.D.; Barnet, C.D.; Wolf, W.W.; Jessup, A.; et al. Ship-Based Measurements for Infrared Sensor Validation during Aerosol and Ocean Science Expedition 2004. *J. Geophys. Res. Atmos.* **2006**, *111*, D09S04. [[CrossRef](#)]
37. Smirnov, A.; Holben, B.N.; Slutsker, I.; Giles, D.M.; McClain, C.R.; Eck, T.F.; Sakerin, S.M.; Macke, A.; Croot, P.; Zibordi, G.; et al. Maritime Aerosol Network as a Component of Aerosol Robotic Network. *J. Geophys. Res. Atmos.* **2009**, *114*. [[CrossRef](#)]
38. Watson, J.G.; Chen, L.W.A.; Chow, J.C.; Doraiswamy, P.; Lowenthal, D.H. Source Apportionment: Findings from the U.S. Supersites Program. *J. Air Waste Manag. Assoc.* **2008**, *58*, 265–288. [[CrossRef](#)] [[PubMed](#)]
39. Cheng, I.; Zhang, L.; Blanchard, P.; Dalziel, J.; Tordon, R. Concentration-Weighted Trajectory Approach to Identifying Potential Sources of Speciated Atmospheric Mercury at an Urban Coastal Site in Nova Scotia, Canada. *Atmos. Chem. Phys.* **2013**, *13*, 6031–6048. [[CrossRef](#)]
40. Kim, J.E.; Kim, I.S.; Won, S.R.; Wee, D. A Simplified Potential Source Density Function Based on Predefined Discretization. *J. Eng. Res.* **2024**. [[CrossRef](#)]
41. Zeng, Y.; Hopke, P.K. A Study of the Sources of Acid Precipitation in Ontario, Canada. *Atmos. Environ.* **1989**, *23*, 1499–1509. [[CrossRef](#)]
42. Stein, A.F.; Draxler, R.R.; Rolph, G.D.; Stunder, B.J.B.; Cohen, M.D.; Ngan, F. NOAA's Hysplit Atmospheric Transport and Dispersion Modeling System. *Bull. Am. Meteorol. Soc.* **2015**, *96*, 2059–2077. [[CrossRef](#)]
43. Hsu, N.C.; Lee, J.; Sayer, A.M.; Kim, W.; Bettenhausen, C.; Tsay, S.C. VIIRS Deep Blue Aerosol Products Over Land: Extending the EOS Long-Term Aerosol Data Records. *J. Geophys. Res. Atmos.* **2019**, *124*, 4026–4053. [[CrossRef](#)]
44. Yu, Y.; Kalashnikova, O.V.; Garay, M.J.; Lee, H.; Notaro, M. Identification and Characterization of Dust Source Regions Across North Africa and the Middle East Using MISR Satellite Observations. *Geophys. Res. Lett.* **2018**, *45*, 6690–6701. [[CrossRef](#)]

45. Di Biagio, C.; Formenti, P.; Balkanski, Y.; Caponi, L.; Cazaunau, M.; Panguì, E.; Journet, E.; Nowak, S.; Caquineau, S.; Andreae, O.M.; et al. Global Scale Variability of the Mineral Dust Long-Wave Refractive Index: A New Dataset of in Situ Measurements for Climate Modeling and Remote Sensing. *Atmos. Chem. Phys.* **2017**, *17*, 1901–1929. [[CrossRef](#)]
46. Kandler, K.; Benker, N.; Bundke, U.; Cuevas, E.; Ebert, M.; Knippertz, P.; Rodríguez, S.; Schütz, L.; Weinbruch, S. Chemical Composition and Complex Refractive Index of Saharan Mineral Dust at Izaña, Tenerife (Spain) Derived by Electron Microscopy. *Atmos. Environ.* **2007**, *41*, 8058–8074. [[CrossRef](#)]
47. El Bamiki, R.; Raji, O.; Ouabid, M.; Elghali, A.; Yazami, O.K.; Bodinier, J.L. Phosphate Rocks: A Review of Sedimentary and Igneous Occurrences in Morocco. *Minerals* **2021**, *11*, 1137. [[CrossRef](#)]
48. Nickovic, S.; Vukovic, A.; Vujadinovic, M.; Djurdjevic, V.; Pejanovic, G. Technical Note: High-Resolution Mineralogical Database of Dust-Productive Soils for Atmospheric Dust Modeling. *Atmos. Chem. Phys.* **2012**, *12*, 845–855. [[CrossRef](#)]
49. Wu, C.; Lin, Z.; Liu, X. The Global Dust Cycle and Uncertainty in CMIP5 (Coupled Model Intercomparison Project Phase 5) Models. *Atmos. Chem. Phys.* **2020**, *20*, 10401–10425. [[CrossRef](#)]
50. Albani, S.; Mahowald, N.M.; Perry, A.T.; Scanza, R.A.; Zender, C.S.; Heavens, N.G.; Maggi, V.; Kok, J.F.; Otto-Bliesner, B.L. Improved Dust Representation in the Community Atmosphere Model. *J. Adv. Model. Earth Syst.* **2015**, *6*, 541–570. [[CrossRef](#)]

**Disclaimer/Publisher’s Note:** The statements, opinions and data contained in all publications are solely those of the individual author(s) and contributor(s) and not of MDPI and/or the editor(s). MDPI and/or the editor(s) disclaim responsibility for any injury to people or property resulting from any ideas, methods, instructions or products referred to in the content.